NEUTRON TOMOGRAPHY STUDIES OF CEMENT-BASED MATERIALS USED FOR RADIOACTIVE WASTE CONDITIONING

S.E. KICHANOV[1], K.M. NAZAROV[1,2], D.P. KOZLENKO[1], M. BALASOIU[1,3*], M. NICU[3], L. IONASCU[3], A.C. DRAGOLICI[3], F. DRAGOLICI[3], B.N. SAVENKO[1]

[1] Frank Laboratory of Neutron Physics, Joint Institute for Nuclear Research, 141980 Dubna, Russia, *E-mail*: ekich@nf.jinr.ru, *E-mail*: denk@nf.jinr.ru, **E-mail*: balas@jinr.ru, *E-mail*: savenko@jinr.ru
[2] State University "Dubna", 141980 Dubna, Russia, *E-mail*: quanysh@list.ru
[3] "Horia Hulubei" National Institute of Physics and Nuclear Engineering, P.O.Box MG-6, Bucharest-Magurele, Romania, *E-mails*: mnicu@nipne.ro, laura_ionascu@nipne.ro, adrag@nipne.ro, fdrag@nipne.ro

Received March 6, 2018

Abstract. The internal structure of several promising cement-based materials for the conditioning of *low and intermediate level radioactive waste* (LILW) were studied using neutron tomography in order to assess the effectiveness and stability of the hardened cement matrix, taking in consideration the need for long term durability in disposal conditions. The spatial distributions of water-containing pores, as well as the arrangement of pores and cracks inside the studied cement-based matrices, were determined on the base of specific interactions of neutrons with various components of the cement samples and the application of modern mathematical algorithms for three-dimensional imaging data analysis. The distributions of the water-containing pores, the lengths and thicknesses of the selected cement-based samples were put in evidence, being a case study for optimizing the concrete matrix to be validated and further applied in the radwaste conditioning.

Key words: Neutron tomography, cement-based materials, pore size distribution, porosity coefficient.

1. INTRODUCTION

Cement-based materials are key elements in the predisposal of radioactive wastes, being widely used in different formulas, in the conditioning phase, either to incorporate the wastes or to prepare the shieldings. Beyond the conditioning phase, they must comply with the disposal waste acceptance criteria (WAC) in terms of stability for 300 y [1, 2]. New methods and formulas of the conditiong matrices are developed for several types of radioactive wastes subject either for long-term storage and / or for disposal in order to improve their anticorrosive and mechanical properties [3–5]. For developing a suitable cement matrix to be used for metallic radioactive aluminium conditioning, the addition of inorganic [6] or organic [7, 8] components into the cement paste were studied [7] in order to reduce the corrosion rate in alkaline solutions and to obtain a low permeability rate. A possible result of incomplete reactions of the compounds or inhomogeneities of the cement paste due

to nonadequate preparation is the formation of cracks or voids inside hardened cement paste [7, 8].

The stringent requirements for the mechanical and chemical properties of cement paste used for radioactive waste conditioning lead to the necessity of conducting several researches and experimental works to study and validate such materials, *i.e.*: (i) X-ray and neutron diffraction, for phase composition and texture evolution; (ii) small angle neutron scattering, for investigation of grains, aggregates or gels inside the cement matrix; (iii) X-ray tomography, for the determination of pore distribution inside the cement matrix [9]. The fundamental differences in the nature of neutron interactions with matter compared to X-rays provides additional benefits to neutron methods, including volumetric studies of massive objects [10], high sensitivity to water distribution [11] inside materials, and notable visual contrast between light element-containing compounds.

Cementitious materials intended for radioactive waste encapsulation usually include substantial amounts of *Ordinary Portland Cement* (OPC) in their formulation. Aluminium is a reactive amphoteric metal, readily forming a protective oxide layer on contact with air or water. This layer is generally regarded as stable in the pH range 4÷10. However, in a strongly alkaline medium, such as that encountered in conventional cementitious materials based on OPC, this layer is soluble, resulting in continued corrosion associated with liberation of hydrogen and subsequent formation of expansive metal hydroxides, in addition to calcium-based aluminosilicate hydrates. As a result, using Portland cement, or a composite cement (OPC blended with blastfurnace slag and/or fly ash) to encapsulate wastes containing aluminium is prohibited.

Recent work [1, 5, 7] has shown that matrices obtained using CEM III-A and CEM V-A (which are commercially available) with addition of different ratio of $Al_2(SO_4)_3$, $C_6H_8O_7$, pantarhol, $LiNO_3$ decrease the pH values and present very good mechanical characteristics, being the based for further investigations.

In the present paper, the results of neutron tomography experiments performed on two types of cements (CEM V and CEM III) are highlighting the evolution of spatial distribution of inner components, as well as the geometric arrangements of pores and voids inside cement matrices, in function of the presence of different admixed compounds. The studies and obtained results are of high value being a base for optimizing the cement matrix formulas, if required.

2. MATERIAL AND METHODS

In the selection and evaluation process of suitable materials for radioactive metallic aluminium conditioning, two sets of samples (presented in Table 1) were prepared based on two types of cement matrices which demonstrate good mechanical behavior, CEM V-A and CEM III-A (see Table 1).

Table 1

The chemical compositions of studied cement samples

Sample label	Sample composition
Sample 1	CEM V + H_2O
Sample 2	CEM V + H_2O+Al (powder)
Sample 3	CEM V + H_2O+Al (powder) + $Al_2(SO_4)_3$ + $C_6H_8O_7$ + pantarhol
Sample 4	CEM V + H_2O+Al (powder) + $Al_2(SO_4)_3$ + $C_6H_8O_7$ + pantarhol + $LiNO_3$
Sample 5	CEM III + H_2O
Sample 6	CEM III + H_2O+Al (powder)
Sample 7	CEM III + H_2O+Al (powder) + $Al_2(SO_4)_3$ + $C_6H_8O_7$ + pantarhol
Sample 8	CEM III + H_2O+Al (powder) + $Al_2(SO_4)_3$ + $C_6H_8O_7$ + pantarhol + $LiNO_3$

The neutron tomography experiments were performed at a neutron radiography and tomography facility [12, 13] placed on the 14th beamline of the high flux pulsed reactor IBR-2. A set of neutron radiography images were collected with a CCD-based detector system with maximal field-of-view of 20×20 cm. The tomography experiments were performed with a rotation step of 0.5º and the total number of measured radiography projections was 360. The exposure time for one projection was 20 s, and resulting measurements lasted for 6 h for each hardened cement sample.

The obtained imaging data were corrected with the camera dark current image and were normalized by the incident neutron beam pattern using the macros developed in our group for the ImageJ software [14]. The tomographic reconstruction was performed using the H-PITRE software [15]. The VGStudio MAX 2.2 software from Volume Graphics (Heidelberg, Germany) was used for the visualization and analysis of reconstructed 3D data. In addition, special plugins for the ImageJ software, including Segmentation3D [16], Local Thickness [17] and Skeletonize3D [18] were used in quantitative analysis of the obtained 3D volume data.

3. RESULTS

Examples of the neutron radiographic images of the cement-based materials used in the tomography reconstruction process are shown in Figure 1. Large amounts of water inside hardened cement samples degrades the quality of the neutron radiograms due to a large amount of incoherent scattering effects. A complex network of cracks and pores contrasts well with the cement based materials in the neutron radiography experiments. A high density of pores and cracks form a complex branched structure, as can be observed in samples 2, 3, 6, and 8. In samples 1, 4, 5 large rounded voids with diameters up to 2÷4 mm are detected.

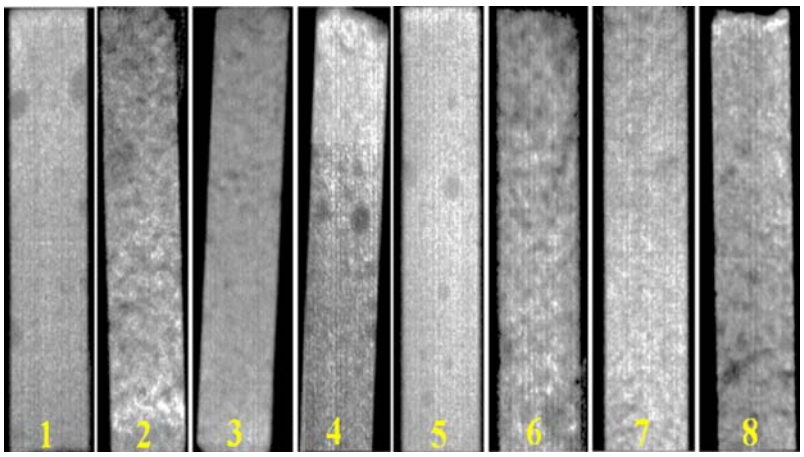

Fig. 1 – The neutron radiography images of the hardened cement samples. The bright regions correspond to high neutron attenuation in the water rich regions inside cement materials. The darker areas are low neutron attenuate regions of the pores and cavities. The background is black.

The 3D models of the studied hardened cement-based samples reconstructed from neutron tomography data are presented in Figure 2. In addition, images representing the transverse sections of the corresponding studied samples are given (Figure 2).

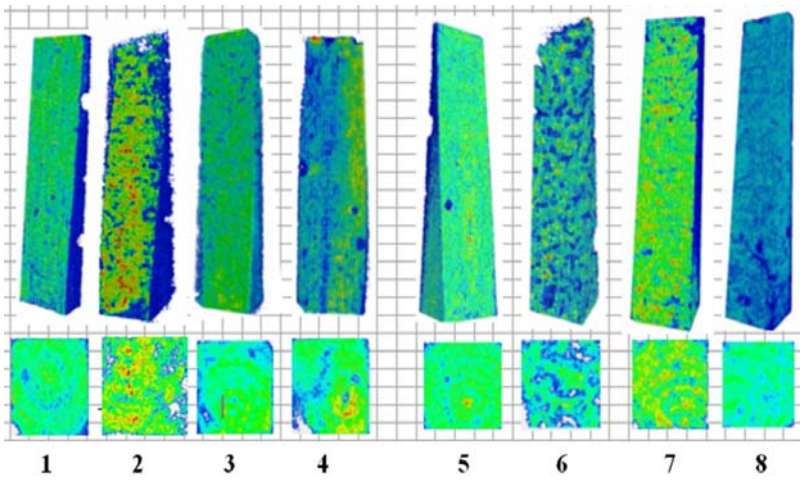

Fig. 2 – The virtual 3D model of the cement samples after the tomographic reconstruction. The virtual beveled cuts of the 3D models are presented for perception improving. The examples of the virtual tomography slices of the studied cement materials, which illustrated a spatial arrangement of cement components. The rainbow-like coloring pattern lies from blue for regions with low neutrons attenuation coefficients to red color for high ones. The red areas correspond to water-rich regions.

An anisotropy of the neutron beam attenuation inside the cement samples is observed. In samples 2, 4, 5 and 7, fine objects characterized by a strong effect of neutron attenuation are easily seen. We can assume that these small formations of different sizes contain free water (because the hydration process are still undergoing) because the neutron attenuation coefficient in water is higher due to the presence of a high incoherent neutron scattering.

The water-containing objects were virtually separated from the 3D models of the hardened cement particles. The volume distributions of separated water-containing pores within samples 2, 4, 5 and 7 are shown in Figure 3. Their characteristic sizes fall in the range of 0.001÷0.1 mm^3. The calculated average volumes of these pores are listed in Table 2.

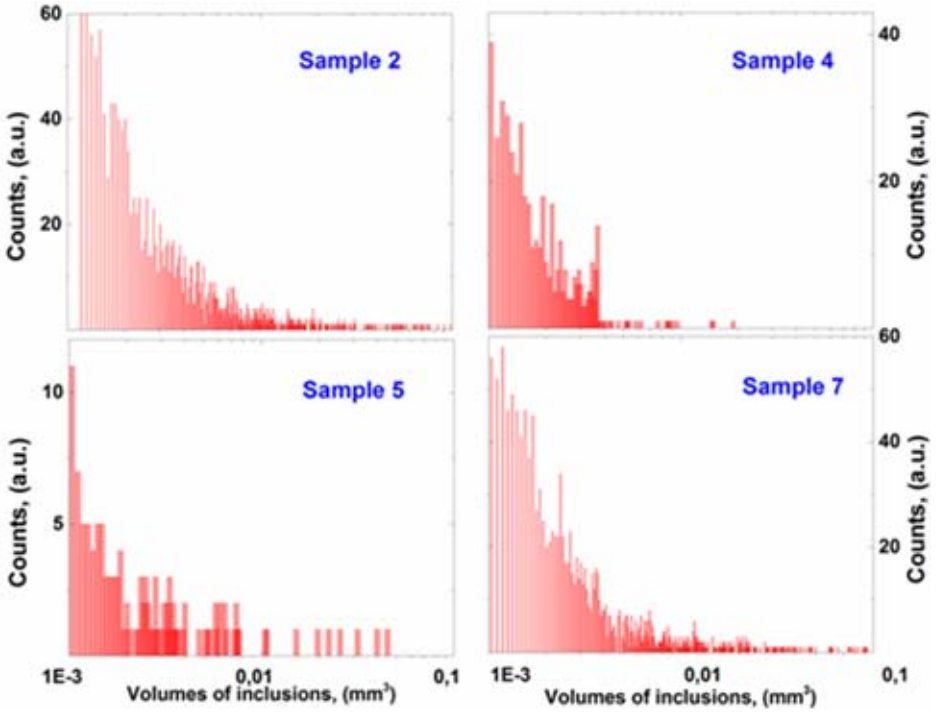

Fig. 3 – The distribution of the estimated volumes of the separated high neutron absorber areas inside the hardened cement samples: Sample 2, 4, 5 and 7.

Table 2

Statistical data of water-rich pore volumes detected inside the investigated cement-based samples

Sample volume	Sample 2	Sample 4	Sample 5	Sample 7
Mean volume, mm^3	0.025(5)	0.003(3)	0.006(3)	0.025(3)
Median volume, mm^3	0.014(3)	0.002(3)	0.003(3)	0.011(5)
Maximum volume, mm^3	0.250(4)	0.02(4)	0.045(5)	0.255(4)

It can be observed that the water-containing pores with relatively larger volumes are present in samples 2 and 7 and these pores form clusters or aggregates with diameters up to 0.6-0.8 mm (Figure 3). At the same time, the distribution of volumes of such pores in the case of samples 4 and 5 shift towards the region of small sizes (Figure 3) and is significantly decreasing.

The final hardened cement-based matrix used for radioactive waste conditioning and long term storage and/or disposal should have a low porosity to prevent radionuclide migration through water infiltration (because in the disposal environment water is considered the main migration vector). The virtual volumes corresponding to pores, cracks, and inner cavities were separated from the total 3D bodies of the cement samples (Figure 4). The calculated parameters for the studied cement matrices are presented in Table 3.

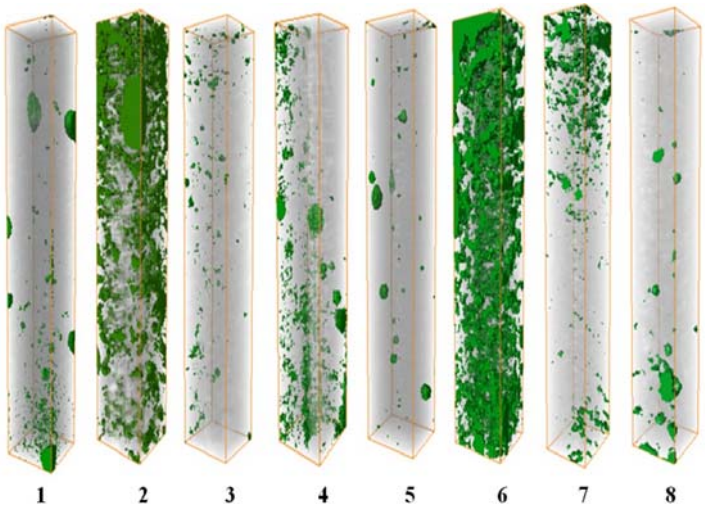

Fig. 4 – The virtual 3D models of the pore and cracks arrangements inside the investigated hardened cement samples based on neutron tomography data.

Table 3

The calculated porosity parameters for the studied cement matrices.
Porosity was calculated as V_{pores}/V_{total} x 100%

Sample label	Porosity, %
Sample 1	1.4
Sample 2	13
Sample 3	1.2
Sample 4	1.8
Sample 5	0.4
Sample 6	16
Sample 7	2.2
Sample 8	0.6

The results presented in Table 3 show that samples 2 and 6 are characterized by high porosity coefficients and complex branched systems of occurred pores and cracks, in contrast to the other samples, where large rounded cavities are present (Figure 1 and Figure 5).

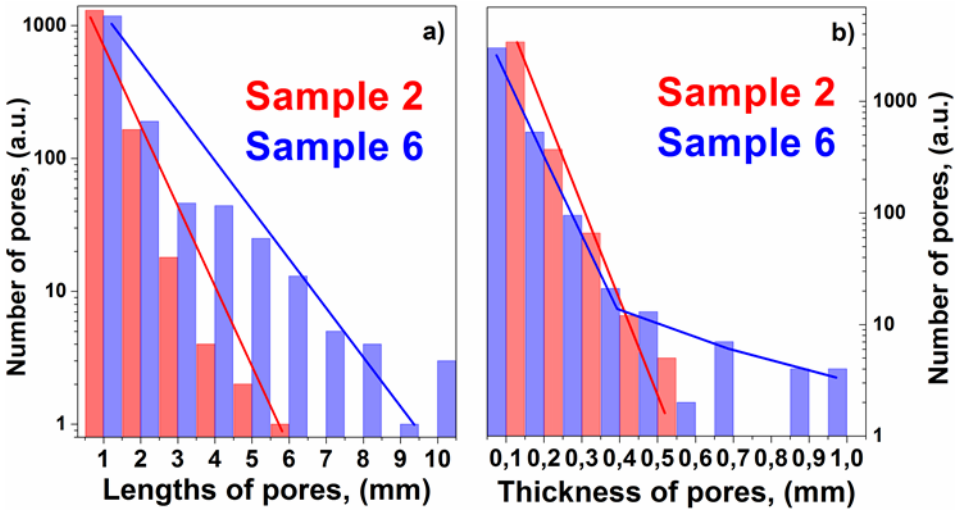

Fig. 5 – a) The distribution of the pore lengths in the calculated skeleton structure of the branched system of pores and cracks inside the cement-based materials: Sample 2 (red bars) and Sample 6 (blue bars). The solid lines are simple linear fits of statistical data. b) The distribution of the pore thicknesses in the calculated skeleton structure of the branched system of pores and cracks inside the cement Sample 2 (red bars) and Sample 6 (blue bars). The solid lines are simple linear and polyline fits of calculated data (Color online).

For the study of the 3D pore network structural features in samples 2 and 6, tomographic models are analysed by means of a skeletonization algorithm [23]. For this method, the connected thread-like pore network is transformed to a 3D skeleton-like dendritic structure [23]. Statistical analysis of the skeleton structures of pores provides distributions of the lengths of the linear parts of the pore network and corresponding thicknesses (Figure 5a–b). If the maximum length of the linear part of pores in sample 2 reaches up to 6 mm, then longer and thicker pores (Figure 5a–b) characterize sample 6. At the same time, the distributions of the lengths and pore thicknesses for sample 6 shift to a larger pore range in comparison to sample 2. This fact indicates a more fractured system of pores and cracks in the sample 6, making a favorable situation for water penetration and consequently a more rapid destruction of the hardened cement matrix.

For comparison with other compositions of the investigated cement-based materials, the distributions of the pore lengths and thicknesses for samples 3 and 7 are displayed in Figure 6a–b. For both these samples, the distribution of length and thickness is shifted noticeably to a smaller size pore region in comparison with

those of samples 2 and 6. The maximum linear length of the pores does not exceed 3.5 mm, and a thickness of 0.6 mm is measured for sample 3. Longer pores with small thicknesses are observed in sample 7. At the same time, shorter and thicker pores are found in sample 3. We can assume that two types of pores are formed in the studied cement-based samples: (i) a branched system of large cracks with sizes from 0.5 to 1.0 mm, and (ii) smaller pores with sizes below 0.4 mm. The large cracks may arise during the solidification process of cement-based materials, while smaller pores are formed due the interaction of the cement-based materials components. Here, the effect of the corrosion process associated with hydrogen generation inside cement matrices can be considered [5, 7, 8] as dominant.

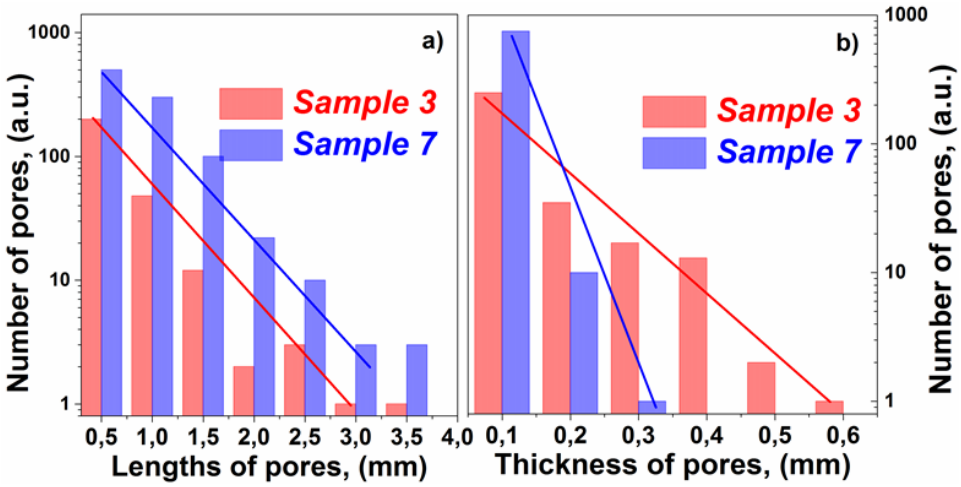

Fig. 6 – a) The distribution of the pore lengths in the calculated skeleton structure of the branched system of pores and cracks inside cement Sample 3 (red bars) and Sample 7 (blue bars). The solid lines are simple linear fits of statistical data. b) The distribution of the pore thicknesses in the calculated skeleton structure of the branched system of pores and cracks inside the cement Sample 3 (red bars) and Sample 7 (blue bars). The solid lines are simple linear fits of calculated data (Color online).

In the future, we intend to continue the investigations on other types of cement-based matrices and new sets of samples to look also specifically at the influence of the preparation technique.

4. CONCLUSIONS

Three-dimensional analysis of two types of cement-based matrices with potential use in radioactive waste conditioning processes was performed by means of neutron tomography. The experimental tomography 3D data were used to analyze the spatial arrangement of pores containing free water and aggregates, as well as inner

pore structures. The obtained structural information is important for understanding the interaction processes between cement components at the micron-scale structural level and can be used to: a) refine the cement-based matrix formulations in order to reduce the possibility of producing pores by using additives, reducing the aluminium content, others, and b) optimize the technological process of manufacturing the cement paste for radioactive waste conditioning, by increasing the mixing time or adding the components in a more adequate manner.

Acknowledgements. This work was supported by the Joint Institute for Nuclear Research (04-4-1121-2015/2020; RO-JINR Projects Nos. 219/10.04.2017 and 220/10.04.2017 item 41).

REFERENCES

1. F. Dragolici, M. Bucataru-Nicu, L. Lungu, C. N. Turcanu, Gh. Rotarescu, Durability of cemented waste in repository and under simulated conditions, IAEA-TECDOC-1397 **137** (2004).
2. J.R. Helliwell, J. Appl. Cryst. **47**, 4–5 (2014).
3. M. Najdoski, V. Koleva, S. Demiri, S. Stojkovikj, Mater. Res. Bull. **47**, 2239–2244 (2012).
4. A.I. Onuchukwu, Materials Chemistry and Physics **20**, 323 (1988).
5. M. Nicu, L. Ionascu, C. Turcanu, F. Dragolici, Rom. J. Phys. **60**, 1193–1202 (2015).
6. T. Matsuo, T. Nishi, M. Matsuda, Trans. Am. Nucl. Soc. **72**, 76 (1995).
7. M. Nicu, L. Ionascu, C. Turcanu, F. Dragolici, Gh. Rotarescu, Rom. J. Phys. **59**, 360–368 (2014).
8. L. Ionascu, M. Nicu, C. Turcanu, F. Dragolici, Gh. Rotarescu, Rom. Rep. Phys. **65**, 1512–1518 (2013).
9. Yan-Shuai Wang, Jian-Guo Dai, NDT & E Int. **86**, 28–35 (2017).
10. I. S. Anderson, R. L. McGreevy, H. Z. Bilheux, *Neutron Imaging and Applications: A Reference for the Imaging Community*, Springer, New York, 2009.
11. H. Justnes, K. Bryhn-Ingebrigtsen, and G.O. Rosvold, Adv. Cem. Res. **6**(22), 67–72 (1994).
12. D.P. Kozlenko, S.E. Kichanov, E.V. Lukin, A.V. Rutkauskas, G.D. Bokuchava, B.N. Savenko, A.V. Pakhnevich, A.Yu. Rozanov, Physics Procedia **69**, 87–91 (2015).
13. D.P. Kozlenko, S.E. Kichanov, E.V. Lukin, A.V. Rutkauskas, A.V. Belushkin, G.D. Bokuchava and B.N. Savenko, Phys. Part. Nuclei Lett. **13**, 346–351 (2016).
14. C.A. Schneider, W.S. Rasband, K.W. Eliceiri, Nat. Methods **9**, 671–675 (2012).
15. R.C. Chen, D. Dreossi, L. Mancini, R. Menk, L. Rigon, T.Q. Xiao, R. Longo, J. Synchrotron Rad. **19**, 836–845 (2012).
16. J. Ollion, J. Cochennec, F. Loll, C. Escude, T. Boudier, Bioinformatics **29**(14), 1840–1841 (2013).
17. R.P. Dougherty, K.H. Kunzelmann, Microscopy and Microanalysis Meeting, USA. **13**, s02, 1678–1679 (2007).
18. T.C. Lee, R.L. Kashyap, C.N. Chu, Comput. Vis. Graph. Image Process. **56**(6), 462–478 (1994).